Theoretical analysis of coupled diffuse-photon-density and thermal-wave field depth profiles photothermally generated in layered turbid dental structures

Anna Matvienko,[1,2,a)] Andreas Mandelis,[1,2] Raymond J. Jeon,[1,2] and Stephen H. Abrams[2]

[1]*Department of Mechanical and Industrial Engineering, Center for Advanced Diffusion-Wave Technologies, University of Toronto, 5 King's College Road, Toronto, Ontario M5S 3G8, Canada*
[2]*Quantum Dental Technologies, 748 Briar Hill Avenue, Toronto, Ontario M6B 1L3, Canada*

A coupled diffuse-photon-density and thermal-wave model is developed for theoretical analysis of the photothermal field in demineralized teeth. Intact and demineralized layers of enamel, as well as dentin, are described as a layered one-dimensional system. The solution of the radiative transport equation in the limit of diffuse-photon-density field is considered as a source term in the thermal-wave field equation. The influence of optical parameters (absorption and scattering coefficients) and thermal parameters (thermal diffusivity and conductivity) of each layer on the diffuse-photon-density and thermal-wave depth profiles is analyzed using computer simulations, allowing the verification of accuracy and validity of the developed theory. The proposed model and simulations are intended for identifying the parameters most affecting the diffuse-photon-density and thermal-wave fields in turbid media, which leads to optimization of the fitting process of thermal and optical properties of teeth from experimental data obtained by frequency-domain photothermal radiometry. © *2009 American Institute of Physics*. [DOI: 10.1063/1.3116128]

I. INTRODUCTION

During the past 3 decades, we have become witnesses to an ever accelerating growth of laser applications, for both clinical treatment and noninvasive diagnostics, in medicine and biology. This is why the processes governing laser-tissue interactions are so thoroughly investigated nowadays. These processes include two main components: optical, i.e., light propagation, and thermal, i.e., energy distribution following optical-to-thermal energy conversion. In order to understand and describe these processes, it is crucial to have accurate information on optical and thermal properties of biological tissues. Moreover, high-resolution noninvasive measurements of optical and thermal properties of tissues can be used as diagnostics of early stages of pathological changes.

Numerous studies have been focused on the *in vivo* evaluation of optical properties of biological tissues. In many cases, these results are based on the radiative transport theory with various modifications (particularly, the diffusion approximation)[1] depending on the applied measurement technique. The main restriction to applications of the diffusion theory is that scattering effects must be significant, which is, however, usually the case with tissues. Particularly, the requirement that the mean free path for photon scattering should be much larger than the wavelength of light and much smaller than the thickness of the medium allows the description of multiply scattered light intensity by means of a diffusion equation.[2] Additional constraints are related to the size of the scattering particles, which should be small compared to the optical wavelength.[2]

A number of diffusion theory variations have been ap-plied for the measurements of optical properties in turbid media. The simple case of the propagation of a uniform diffuse irradiance through a one-dimensional medium is described by the Kubelka–Munk theory,[3] which is equivalent to a diffusion model having forward and backward scattered optical fluxes. The model calculates absorption and scattering coefficients from measurements of diffuse reflectance and transmittance. However, this method is strongly limited in its accuracy, mainly due to the unrealistic condition of perfectly diffuse light source.[4]

Another group of methods apply inverse adding-doubling algorithm[5,6] for the calculation of absorption and scattering characteristics from experimental data on reflectance and transmittance, which can be obtained with single- or double-integrating sphere techniques.[7–9] These methods are based on the numerical solution of the radiative transport equation and involve a prediction-correction procedure for the calculation of optical coefficients. The methods are fast and accurate, but the pertinent experimental data are usually obtained *in vitro*.

Another model used for calculations of optical properties from experimental results is the Monte Carlo approach, which describes pathways of photons in the material on a random basis.[10] This method can be applied to samples with any absorption-to-scattering coefficient ratio, but the long time required for calculations restricts its efficiency. The Monte Carlo based techniques[11–13] are accurate and robust, and do not require limiting simplifications, but complexity and very extensive calculations significantly reduce the efficiency of the optical evaluation. The method involves an iterative procedure of adjustment of calculated optical prop-

a)Author to whom correspondence should be addressed. Electronic mail: ann@mie.utoronto.ca.

erties according to the Monte Carlo modeled predictions for the data on diffuse or collimated reflectance and transmittance.

The diffusion approximation and the Monte Carlo approach are the most popular methods used in the evaluation of tissue optical properties. There are some other models reported in the literature, such as the random-walk model, which is based on representing photon movement by a random walk on a lattice.[14] As in diffusion theory, this model is applicable mostly to low-absorption media. However, it is more computational than physical, so it is rarely used in tissue optics. More fundamental analyses are based on analytical solutions to Maxwell's equations and take into account the statistical character of photon propagation in turbid media.[15] This complicated theory is hardly ever used in tissue evaluation due to the limited possibilities for experimental implementation.

In addition, there are several other approximate models reported in the literature such as the empirical light transport model[16] or multidirectional flux approximations.[17,18] These models represent scattered light as fluxes in multiple directions. The resulting system of equations is then solved numerically with a finite difference method to obtain tissue properties.

All techniques mentioned above are continuous wave and are based on the spatial dependence of reflectance and transmittance; the latter is usually measured *in vitro* or, at least, invasively. For *in vivo* measurements, the spatially resolved, steady-state reflectance[19,20] was analyzed based on the diffusion approximation and results were compared with Monte Carlo simulations. It was noted that the results obtained with both methods show a good fit when multiply scattered light is measured. So the computationally fast diffusion theory is preferable in this case. The lattice random-walk theory was applied[14] to derive the expression for radial reflectance distribution. These methods, however, still require another independent determination of one of the optical properties. In addition, the absolute measurements of radial reflectance can be easily affected by instrumentation elements, reducing the reliability of the data.[20]

Other families of *in vivo*, noninvasive techniques are based on time-resolved reflectance data,[21,22] frequency-domain reflectance measurements,[23] a photon time-of-flight method,[24,25] laser-induced stress transient (optoacoustic or photoacoustic) detection,[26,27] laser-induced thermal transient detection (pulsed photothermal radiometry),[28–30] as well as a frequency-domain evaluation of laser-induced thermal effects in tissues—frequency-domain photothermal radiometry of soft tissues[31] and of hard tissues.[32,33]

The group of photothermal methods is intended not only for optical tissue evaluation but also they have distinct advantages for biomedical imaging and diagnosis due to their noninvasive character. Among them, coupled-field (photoacoustic and photothermal) techniques recently attracted much attention since the energy-converted (acoustic or thermal) signal detection can significantly increase resolution and contrast with respect to pure optical diagnostics and imaging, and allows comprehensive and simultaneous analysis of, for example, optical and thermal properties of tissue dur-

ing photothermal measurements. This type of analysis is inevitably necessary for a majority of laser-tissue interaction processes.

The two aforementioned photothermal techniques, namely, pulsed- and frequency-domain radiometry, are based on the thermal infrared response of a medium to a single-pulse (or frequency-modulated) laser irradiation following optical-to-thermal energy conversion. The generated signals carry subsurface information in the form of a temperature depth integral, allowing analysis of the medium well below the range of optical imaging. Based on the measured infrared signal, both optical and thermal characteristics of tissues can be evaluated noninvasively. Pulsed photothermal radiometry was applied to various tissue measurements, including dental enamel.[34,35] However, the temporal decay of the thermal pulse represents only one signal channel available to analysis, requiring an additional independent optical measurement to extract a reliable set of optical parameters.[29]

Frequency-domain photothermal radiometry provides two signal channels (amplitude and phase). In this method, a harmonically modulated laser beam generates diffuse-photon-density waves in a turbid medium. Following photon migration (diffusion) and scattering, the absorbed fraction of the diffusive light creates an oscillatory temperature (thermal-wave) field, which is detected radiometrically. Diffuse-photon-density waves are scalar, damped, traveling waves of light energy density.[36,37] This kind of highly damped traveling waves arises formally in any diffusive system that is driven by an oscillating force, such as intensity-modulated light. A number of analytical studies were focused on the diffuse-photon-density-wave optics in turbid media.[38–43] Although microscopically the photons are diffusing and have thus lost their coherence and memory of their initial direction, macroscopically they add incoherently to produce a scalar wave of light energy density with a well-defined phase front. The wavelength of the diffuse-photon-density wave depends on the optical properties and the modulation frequency of the incident light.[40] It will be shown further on that at very low modulation frequencies compared with the inverse of the diffuse-photon absorption time constant $\tau = 1/\nu\mu_a$ (ν is the speed of light in a tissue medium), the diffuse-photon-density-wave mathematical formalism loses its oscillating character, and the dc limit of the photon field transport equation can be considered.[44]

The diffusion theory, applied in the aforementioned studies, was proven to be effective and accurate, and computationally fast compared to Monte Carlo simulations. However, the diffusion approximation has certain limitations. It was pointed out[1] that when the optical beam enters turbid media, first order scattering is dominant near the surface, and as the observation point moves into the medium, more and more secondary scattering events take place. The diffusion solution is an approximation representing the limiting case where multiple scattering is dominant. It is, therefore, clear that near the surface the diffusion solution may not be applicable. The limitations of the diffusion approximation with respect to the scattering/absorption abilities and particle size of a turbid medium have been thoroughly investigated.[2] The authors demonstrated that, for most scattering media, diffusion

theory gives good agreement with experimental data for depths greater than the ballistic photon region (μ_s^{-1}, where μ_s is the scattering coefficient), but only if particles are small compared to the optical wavelength. For scatterers that are large compared to the optical wavelength, diffusion theory is applicable only when the optical absorption depth is large compared to the ballistic photon region. For media with significant absorption, the diffusion theory is also not valid.[2] Therefore, Monte Carlo simulations would be preferable for the interpretation of the optical profiles in these conditions.

With regard to healthy dental enamel, the ballistic photon region is expected to be up to $\mu_s^{-1} \approx 0.16$ mm for scattering coefficient values ~ 6000 m^{-1} (at 632 nm laser wavelength),[45] while the size of enamel crystals (30–40 nm in diameter[46]) is much less than the range of laser light wavelengths in the optical window range of tissue (700–1500 nm). Moreover, in the case of *in vivo* dental enamel, the thickness of enamel is about one to several millimeters, which is much thicker than the ballistic region. Appropriate boundary conditions must be applied to ensure optical energy conservation principles at the turbid medium surface, if the diffusion approximation is used. A major advantage of the diffusion approximation is that when it comes to coupled optical and thermal-wave fields, such as in photothermal detection and analysis, lengthy Monte Carlo optical calculations become even less efficient compared to computationally fast diffusion calculations.

The complete theoretical formalism of photothermal radiometry includes the description of two fields: optical and thermal. For pulsed photothermal radiometry, a coupled analysis of these fields has been introduced.[29] The authors considered the one-dimensional diffusion approximation for the absorbing and scattering optical fields and the Green function approach for the heat conduction equation in a homogeneous turbid medium. The model was applied for the measurement of optical properties of samples, while the thermal properties were known. A similar analysis for the simpler case of only absorbing (but not scattering) tissue has been applied to the thermal diffusivity evaluation of skin with known optical properties.[47] These studies demonstrated the important potential of photothermal radiometry as a novel tool for *in vivo* thermal analysis of tissues, which is traditionally done with invasive methods such as by means of the measurement of thermal response with a set of sensor probes inserted into tissues.[48]

A method for noninvasive simultaneous optical and thermal characterization of turbid media has been introduced,[44,49] in which the authors developed a rigorous three-dimensional model for frequency-domain photothermal radiometry, where the diffuse-photon-density field in the laser-irradiated tissue acts as a modulated source for the thermal-wave field. This method was later applied for the optical and thermal evaluation of homogeneous dental enamel.[33] However, in many cases biological tissues such as skin, teeth, etc., are not homogeneous. For example, a demineralized tooth has layered structure comprising demineralized enamel, intact enamel, dentin, and pulp. There are a number of studies on the optical evaluation of a layered medium. Steady-state, time-resolved, and frequency-domain op-
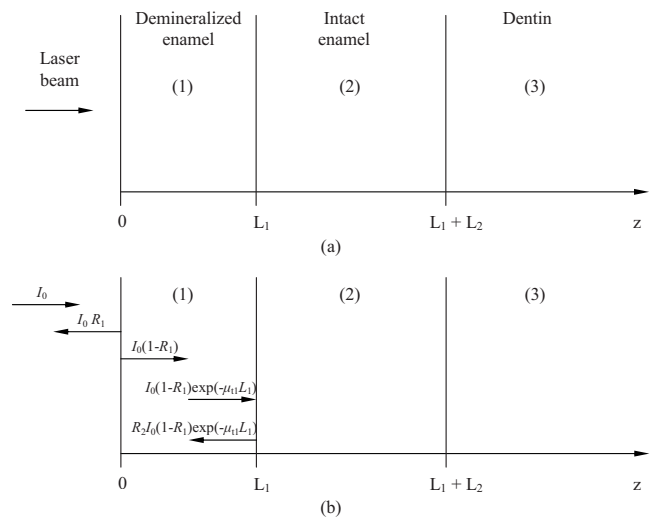

FIG. 1. (a) Three-layer one-dimensional model of a demineralized tooth section. (b) Inter-reflection scheme inside the upper tooth layer formed by a demineralizing agent.

tical fields in a two-layer turbid medium have been examined with the diffusion approximation.[50–53] In addition, a random-walk model,[54] as well as numerical solution of the diffusion equation[55] have been reported. Good potential for estimating the optical properties and/or the layered structure of tissue has been demonstrated using the diffusion approximation theory fitted to measured[50,51] or Monte Carlo simulated[52,56,57] reflectance data. A Fourier transform based solution within the diffusion approximation was presented for a three-layered medium.[58] The applied approach was a followup to a two-layered tissue analysis.[52,59] The authors calculated depth profiles and time-domain dependence of reflectance for a layered matched medium and compared the results to the Monte Carlo generated reflectance profiles. They concluded that for many applications the reflectance calculated with diffusion equations with appropriate boundary conditions is exact enough to replace the time-consuming Monte Carlo simulations.

To our best knowledge, there have been no attempts in the literature to describe coupled diffuse-photon-density wave and thermal-wave fields for the photothermal radiometric analysis of layered tissues. In this paper, we expand the theoretical formalism developed for the frequency-domain photothermal radiometry of a single-layer turbid medium to the three-layer case with appropriate boundary and interfacial conditions and show the capabilities of the model to describe diffuse-photon-density and thermal-wave profiles as functions of the layer properties. The motivation for these studies is the assessment of the capabilities of photothermal radiometry to monitor quantitatively the demineralization of dental enamel by acidic agents contained in food and drinks as well as through the action of bacteria.

II. THEORETICAL MODEL OF COUPLED DIFFUSE-PHOTON AND THERMAL-WAVE FIELDS

A. Diffuse and coherent photon fields

We assume that a three-layered one-dimensional turbid structure is irradiated with laser light [Fig. 1(a)]. As a result

of the incident radiation, a one-dimensional total photon field density Ψ_t arises inside the medium. It can be divided into two components:

$$\Psi_{t_i}(z;\omega) = \Psi_{c_i}(z;\omega) + \Psi_{d_i}(z;\omega), \tag{1}$$

where Ψ_{c_i} is the coherent photon density and Ψ_{d_i} is the diffuse-photon density of the turbid medium. The contribution of the coherent term to the diffuse-photon-density field compensates for the absence of ballistic photon regime in the very-near-surface region in the radiative transport diffusion approximation theory. Here, the subscript i denotes (1) demineralized layer, (2) intact enamel, and (3) dentin. The depth profiles of the optical and thermal fields (see Sec. III) show significant changes only up to a certain depth in hard dental tissue, which is usually less than 3–4 mm with calculations based on the literature values of the thermal and optical pa-

rameters of teeth. The thickness of human dental enamel varies from 0.8 to 1. 95 mm (Ref. [60]) and the dentin thickness varies from about 4 to 9 mm.[61] Therefore, in practice the combined layer would definitely be thicker than 3–4 mm. Based on this fact, the model does not involve the pulp layer, which may be too deep to matter in the spectral range of our experiments.

The one-dimensional coherent photon-density field takes into account the reduction in the incident intensity due to scattering and absorption:

$$\Psi_{c_1} = \frac{I_0(1-R_1)\{\exp[-\mu_{t_1}z] + R_2\exp[-\mu_{t_1}(2L_1-z)]\}}{1-R_1R_2\exp[-2\mu_{t_1}L_1]},$$

$$\Psi_{c_2} = \frac{I_0(1-R_1)(1+R_2)\exp[-\mu_{t_1}L_1]\exp[-\mu_{t_2}(z-L_2)]}{1-R_1R_2\exp[-2\mu_{t_1}L_1]},$$

$$\Psi_{c_3} = \frac{I_0(1-R_1)(1+R_2)\exp[-(\mu_{t_1}L_1+\mu_{t_2}L_2)]\exp\{-\mu_{t_3}[z-(L_1+L_2)]\}}{1-R_1R_2\exp[-2\mu_{t_1}L_1]}, \tag{2}$$

where I_0 is the laser intensity, R_1 is the reflectivity of the outermost turbid medium (demineralized enamel), R_2 is the reflectivity of the healthy enamel layer, and

$$\mu_{t_i} = \mu_{a_i} + \mu_{s_i}. \tag{3}$$

Here, μ_t is the total attenuation coefficient of layer i, which includes the absorption coefficient μ_a (m^{-1}) and the scattering coefficient μ_s (m^{-1}) of the medium.

The internal inter-reflection effect is taken into account only in the demineralized layer, since the optical diffusion depth $\mu_{s_1}^{-1}$ may become commensurate with the thickness of the layer. Indeed, the scattering coefficient of healthy enamel is approximately equal to $\mu_s = 6000$ m^{-1},[45] but its value may increase up to three to four times in demineralized zones [$\mu_s = 19\,000$ m^{-1} at 91% mineral content (Ref. [46])]. This leads to the decrease in the optical diffusion depth $\mu_{s_1}^{-1}$ from 0.16 mm to several tens of microns, the thickness which is of the order of magnitude of incipiently demineralized layers.[62] In healthy enamel and dentin layers, the optical diffusion depth μ_s^{-1} is much smaller than the average thickness of the layers, so the effect of the inter-reflections between boundaries becomes negligible beyond the uppermost layer.

In its general form, the one-dimensional diffuse-photon-density equation in the frequency domain can be described as[49]

$$\frac{d^2}{dz^2}\Psi_{d_i}(z;\omega) - \sigma_{d_i}^2\Psi_{d_i}(z;\omega) = -\frac{1}{D_i}G_i(z;\omega), \quad i=1,2,3, \tag{4}$$

where the complex diffuse-photon-wave number is defined as[38]

$$\sigma_d^2 = \frac{1-i\omega\tau}{\nu D\tau}. \tag{5}$$

Here, τ is a statistical photon lifetime which is limited by an absorption event. $D = 1/3\mu_t'$ is the optical diffusion coefficient (m), and

$$\mu_t' = \mu_a + (1-g)\mu_s \tag{6}$$

is the reduced attenuation coefficient. g is the mean cosine of the scattering angle. D represents the mean free path of photons limited by absorption and scattering. For tissues, the reduced attenuation coefficient μ_t' [Eq. (6)] is much smaller than the total attenuation coefficient μ_t [Eq. (3)] due to the high value of the mean cosine of the scattering angle g, which is close to unity for highly scattering turbid media.[1] The function G represents a photon source[38] and will be defined below.

In the usual photothermal experimental modulation frequency range (≤ 1 MHz), the wave nature of the photon field is immaterial, so Eq. (4) can be replaced by the dc approximation under on-off modulation conditions. This approach is valid if the angular modulation frequency ω is significantly lower than the inverse of the diffuse-photon absorption lifetime, $\omega \ll \tau^{-1}$, so the complex photon-wave number equation (5) becomes real

$$\sigma_d^2 \approx 3\mu_a\mu_t' \equiv Q^2. \tag{5'}$$

In the case of diffusion-photon-wave propagation in tissues, a typical value of the inverse diffuse-photon absorption lifetime is $\nu\mu_a \approx 10^9$ Hz.[38] Therefore, we adopt the dc form of the diffuse-photon-density field (Eq. (4)):[44]

TABLE I. Optical (632 nm) and thermal properties of dental tissues (Refs. [45], [63], and [64]).

	Optical absorption coefficient μ_a (m^{-1})	Optical scattering coefficient μ_s (m^{-1})	Thermal diffusivity α (m^2/s)	Thermal conductivity κ (W/mK)
Enamel	<100	6000 ± 1800	$(4.2-4.69) \times 10^{-7}$	0.913–0.926
Dentin	300–400	$28\,000 \pm 8400$	$(1.87-2.6) \times 10^{-7}$	0.577–0.623

$$\frac{d^2}{dz^2}\Psi_{d_i}(z) - 3\mu_{a_i}\mu'_{t_i}\Psi_{d_i}(z) = -\frac{1}{D_i}G_i(z), \qquad (7)$$

where the function G_i is given by

$$G_i(z) = \mu_{s_i}\left(\frac{\mu_{t_i} + g\mu_{a_i}}{\mu_{t_i} - g\mu_{s_i}}\right)\Psi_{c_i}. \qquad (8)$$

The general solutions for the optical fields for each layer ($i = 1, 2, 3$), including coherent and diffuse components, can be written as

$$\Psi_{t_1}(z) = a_1 \exp(Q_1 z) + b_1 \exp(-Q_1 z) + I_{\text{eff}}(1 + C_{\mu 1})$$
$$\times \{\exp[-\mu_{t_1}z] + R_2 \exp[-\mu_{t_1}(2L_1 - z)]\}, \quad (9a)$$

$$\Psi_{t_2}(z) = a_2 \exp[Q_2(z - L_1)] + b_2 \exp[-Q_2(z - L_1)]$$
$$+ I_{\text{eff}}(1 + R_2)(1 + C_{\mu 2})\exp(-\mu_{t_1}L_1)$$
$$\times \exp[-\mu_{t_2}(z - L_1)], \qquad (9b)$$

$$\Psi_{t_3}(z) = b_3 \exp\{-Q_3[z - (L_1 + L_2)]\}$$
$$+ I_{\text{eff}}(1 + R_2)(1 + C_{\mu 3})\exp[-(\mu_{t_1}L_1 + \mu_{t_2}L_2)]$$
$$\times \exp\{-\mu_{t_3}[z - (L_1 + L_2)]\}, \qquad (9c)$$

where the integration constants due to the coherent field solutions are given by

$$C_{\mu_i} = \frac{3\mu_{s_i}(\mu_{t_i} + g\mu_{a_i})}{3\mu_{a_i}\mu'_{t_i} - \mu^2_{t_i}},$$

$$I_{\text{eff}} = \frac{I_0(1 - R_1)}{1 - R_1 R_2 \exp(-2\mu_{t_1}L_1)}. \qquad (10)$$

In Eq. (9) Q_i are defined as $Q_i = \sqrt{3\mu_{a_i}\mu'_{t_i}}$. It should be mentioned here that for the case of dentin, the dc photon diffusion depth[38] $\sqrt{D/\mu_a} = \sqrt{1/(3\mu_a\mu'_t)}$ is about 0.6 μm (literature values for the properties of dental tissues are listed in Table I), which is much less than the dentin layer thickness. Therefore, a semi-infinite assumption will be valid for the dentin layer in Eq. (9), as shown in Fig. 1.

The boundary conditions are of the so-called "third-kind" at the air-tooth interface, as well as continuity of photon-density field and photon flux at the interfaces between solid layers. They can be written as follows:

$$\Psi_{d_1}(0) = A\frac{d}{dz}\Psi_{d_1}(z)\big|_{z=0}, \qquad (11a)$$

$$\Psi_{d_1}(L_1) = \Psi_{d_2}(L_1) \qquad (11b)$$

$$D_1\frac{d}{dz}\Psi_{d_1}(z)\big|_{z=L_1} = D_2\frac{d}{dz}\Psi_{d_2}(z)\big|_{z=L_1}, \qquad (11c)$$

$$\Psi_{d_2}(L_1 + L_2) = \Psi_{d_3}(L_1 + L_2), \qquad (11d)$$

$$D_2\frac{d}{dz}\Psi_{d_2}(z)\big|_{z=L_1+L_2} = D_3\frac{d}{dz}\Psi_{d_3}(z)\big|_{z=L_1+L_2}. \qquad (11e)$$

Here, the constant A is defined as[19]

$$A = 2D\left(\frac{1 + r}{1 - r}\right), \qquad (12)$$

where r is the internal reflection of uniformly diffusing radiation, which depends on the index of refraction of the sample.[28] Solving the system of the five equations of the boundary conditions using the photon diffusion field equations (9) and the coherent equations (2) in Eq. (1), one can obtain the coefficients a_1, a_2, b_1, b_2, and b_3:

$$a_1 = \frac{-d_1 P - f_1 N \exp(-2\mu_{t_1}L_1) - \dfrac{(2VF + G)\exp(Q_1 L_1)}{(1 + X_{12} - 2VX_{12})}}{M - \dfrac{(1 - X_{12} + 2VX_{12})\exp(2Q_1 L_1)}{(1 + X_{12} - 2VX_{12})}},$$

$$b_1 = -a_1 M - d_1 P - f_1 N \exp(-2\mu_{t_1}L_1),$$

$$a_2 = b_2 + d_2 Y_{22} + X_{12}a_1 \exp(Q_1 L_1) - X_{12}b_1 \exp(-Q_1 L_1)$$
$$+ Y_{12}(f_1 - d_1)\exp(-\mu_{t_1}L_1),$$

$$b_2 = VF - VX_{12}a_1 \exp(Q_1 L_1) + VX_{12}b_1 \exp(-Q_1 L_1)$$

$$b_3 = -a_2 X_{23} \exp(Q_1 L_1) + b_2 X_{23} \exp(-Q_1 L_1)$$
$$+ Y_{23}d_2 \exp(-\mu_{t_2}L_2) - Y_{33}d_3. \qquad (13)$$

Here, the parameters M, N, P, X, Y, and d are defined as

$$M \equiv \frac{1 - Q_1 A}{1 + Q_1 A}, \quad N \equiv \frac{1 - \mu_{t_1}A}{1 + Q_1 A}, \quad P = \frac{1 + \mu_{t_1}A}{1 + Q_1 A},$$

$$X_{ij} \equiv \frac{D_i Q_i}{D_j Q_j}, \quad Y_{ij} \equiv \frac{D_i \mu_{t_i}}{D_j Q_j},$$

$$d_1 = C_{\mu_1}I_{\text{eff}}, \quad f_1 = d_1 R_2,$$

$$d_2 = C_{\mu_2}I_{\text{eff}}(1 + R_2)\exp(-\mu_{t_1}L_1),$$

$$d_3 = C_{\mu_3} I_{eff} (1 + R_2) \exp[-(\mu_{t_1} L_1 + \mu_{t_2} L_2)]. \tag{14}$$

The coefficients F, G and V are defined as

$$F = d_2 \frac{\exp(-\mu_{t_2} L_2)(Y_{23} - 1)}{\exp(Q_2 L_2)(X_{23} + 1)} + d_3 \frac{\exp(1 - Y_{33})}{\exp(Q_2 L_2)(X_{23} + 1)}$$
$$- d_2 Y_{22} - (f_1 - d_1) Y_{12} \exp(-\mu_{t_1} L_1)$$

$$G = -(f_1 + d_1) \exp(-\mu_{t_1} L_1) + d_1 + d_2 Y_{22} + (f_1$$
$$- d_1) Y_{12} \exp(-\mu_{t_1} L_1),$$

$$V = \frac{1}{1 - \dfrac{(X_{23} - 1)}{(X_{23} + 1)} \exp(-2 Q_2 L_2)}. \tag{15}$$

B. Thermal-wave field

The total diffuse-photon-density field Ψ_t is a source of the much more slowly propagating thermal-wave field given by

$$\frac{d^2}{dz^2} T_i(z; \omega) - \sigma_i^2 T_i(z; \omega) = -\eta_{NR} \frac{\mu_{a_i}}{\kappa_i} \Psi_{t_i}(z; \omega), \quad i = 1, 2, 3, \tag{16}$$

where

$$\sigma_i = \sqrt{\frac{i\omega}{\alpha_i}} \tag{17}$$

is the thermal wavenumber $(\mathrm{m^{-1}})$, which depends on the modulation frequency and on thermal diffusivity α $(\mathrm{m^2\,s^{-1}})$ of ith layer. Here, η_{NR} is the nonradiative efficiency and κ is the thermal conductivity of the ith layer $(\mathrm{W\,m^{-1}\,K^{-1}})$.

Taking into account the semi-infinite character of the dentin layer, the thermal-wave fields for each layer can be written in the forms

$$T_1(z; \omega) = A_1 \exp(\sigma_1 z) + B_1 \exp(-\sigma_1 z) + C_1 \exp(Q_1 z)$$
$$+ D_1 \exp(-Q_1 z) + E_1 \exp(-\mu_{t_1} z)$$
$$+ F_1 \exp[-\mu_{t_1}(2L_1 - z)], \tag{18a}$$

$$T_2(z; \omega) = A_2 \exp[\sigma_2(z - L_1)] + B_2 \exp[-\sigma_2(z - L_1)]$$
$$+ C_2 \exp[Q_2(z - L_1)] + D_2 \exp[-Q_2(z - L_1)]$$
$$+ E_2 \exp[-\mu_{t_2}(z - L_1)], \tag{18b}$$

$$T_3(z; \omega) = B_3 \exp\{-\sigma_3[z - (L_1 + L_2)]\} + D_3 \exp\{-Q_3[z$$
$$- (L_1 + L_2)]\} + E_3 \exp\{-\mu_{t_3}[z - (L_1 + L_2)]\}. \tag{18c}$$

Again, the dentin layer is considered semi-infinite, since the thermal diffusion depth, for example, at 1 Hz is $\sqrt{2\alpha_3/\omega}$ $= 0.29$ mm (the dentin properties are listed in Table I), which is much less than the dentin thickness. The coefficients C_i, D_i, E_i, and F_i are defined as

$$C_i = -\frac{\eta_{NR_i} \mu_{a_i}}{\kappa_i (Q_i^2 - \sigma_i^2)} a_i, \quad i = 1, 2,$$

$$D_i = -\frac{\eta_{NR_i} \mu_{a_i}}{\kappa_i (Q_i^2 - \sigma_i^2)} b_i, \quad i = 1, 2, 3,$$

$$E_i = -\frac{\eta_{NR_i} \mu_{a_i}}{\kappa_i (\mu_{t_i}^2 - \sigma_i^2)} d_i, \quad i = 1, 2, 3,$$

$$F_1 = -\frac{\eta_{NR_i} \mu_{a_i}}{\kappa_i (\mu_{t_i}^2 - \sigma_i^2)} f_1. \tag{19}$$

Here, a_i, b_i, d_i, and f_1 are given in Eqs. (13) and (14). To determine the coefficients A_i and B_i, the following boundary conditions are used:

$$\kappa_1 \frac{dT_1(z, \omega)}{dz} \bigg|_{z=0} = H T_1(0; \omega), \tag{20a}$$

$$T_1(L_1, \omega) = T_2(L_1, \omega), \tag{20b}$$

$$\kappa_1 \frac{dT_1(z, \omega)}{dz} \bigg|_{z=L_1} = \kappa_2 \frac{dT_2(z, \omega)}{dz} \bigg|_{z=L_1}, \tag{20c}$$

$$T_2(L_1 + L_2, \omega) = T_3(L_1 + L_2, \omega) \tag{20d}$$

$$\kappa_2 \frac{dT_2(z, \omega)}{dz} \bigg|_{z=L_1+L_2} = \kappa_3 \frac{dT_3(z, \omega)}{dz} \bigg|_{z=L_1+L_2}. \tag{20e}$$

As a result, the coefficients of the photothermal fields T_1, T_2, and T_3 in Eqs. (18) can be found from the solution of the following system of equations:

$$A_1(1 - b_{01}) - B_1(1 + b_{01})$$
$$= C_1(b_{01} - q_{11}) + D_1(b_{01} + q_{11}) + E_1(b_{01} + m_{11})$$
$$+ F_1 \exp(-\mu_{t_1} L_1)(b_{01} - m_{11}),$$

$$A_1 \exp(\sigma_1 L_1) + B_1 \exp(-\sigma_1 L_1) - A_2 - B_2$$
$$= C_2 + D_2 + E_2 - C_1 \exp(Q_1 L_1) - D_1 \exp(-Q_1 L_1)$$
$$- (E_1 + F_1) \exp(-\mu_{t_1} L_1),$$

$$b_{12} A_1 \exp(\sigma_1 L_1) - b_{12} B_1 \exp(-\sigma_1 L_1) - A_2 + B_2$$
$$= q_{22} C_2 - q_{22} D_2 - m_{22} E_2 - q_{12} C_1 \exp(Q_1 L_1)$$
$$+ q_{12} D_1 \exp(-Q_1 L_1) - m_{12}(F_1 - E_1) \exp(-\mu_{t_1} L_1),$$

$$A_2 \exp(\sigma_2 L_2) + B_2 \exp(-\sigma_2 L_2) + B_3$$
$$= -C_2 \exp(Q_2 L_2) - D_2 \exp(-Q_2 L_2)$$
$$- E_2 \exp(-\mu_{t_2} L_2) - D_3 - E_3,$$

$$q_{23}A_2 \exp(\sigma_2 L_2) - q_{23}B_2 \exp(-\sigma_2 L_2) + B_3$$
$$= -q_{23}C_2 \exp(Q_2 L_2) + q_{23}D_2 \exp(-Q_2 L_2)$$
$$+ m_{22}E_2 \exp(-\mu_{t_2} L_2) - q_{33}D_3 - m_{33}E_3, \qquad (21)$$

where the following definitions are used:

$$b_{ij} \equiv \frac{\kappa_i \sigma_i}{\kappa_j \sigma_j}, \quad q_{ij} \equiv \frac{\kappa_i Q_i}{\kappa_j \sigma_j}, \quad m_{ij} \equiv \frac{\kappa_i \mu_{t_i}}{\kappa_j \sigma_j}. \qquad (22)$$

III. DIFFUSE-PHOTON AND THERMAL-WAVE FIELD SIMULATIONS

Theoretical simulations of the total diffuse-photon field [Eq. (9)] and the thermal-wave field [Eq. (18)] were performed to show the influence of thermal and optical parameters of the layers of dental tissue (see the literature values in Table I) on the field distributions. This exercise is crucial for understanding the importance of every parameter in the inevitably multiparameter analysis of the photothermal signals. It is obvious from the mathematical structure of Eqs. (9) and (18) that some tissue properties have stronger impact than others on the photon-wave and thermal-wave propagation through a medium. Identifying those groups of parameters will help strengthen multiparameter fits by fixing some variables which do not affect the field distribution significantly, thus reducing the degrees of freedom and computational time in the fitting procedure. Recalling that the three-layer theoretical model has more than 20 parameters, most of which are unknown, one can immediately comprehend the value of identifying as many minor variables as possible.

While the thermal-wave field is both coordinate and frequency dependent, the diffuse-photon field is inherently a dc field in the frequency range of our experiments and is spatially distributed only. Since thermal properties do not influence photon propagation in the narrow temperature range of our experiments, the diffuse-photon-field analysis is further reduced to the demonstration of the role of optical parameters of the various layers in the resulting photon field distribution.

A. Depth profile dependence on the optical absorption coefficient

Figure 2 shows the depth profile of the diffuse-photon (a) and thermal-wave [(b) and (c)] fields for various absorption coefficients of the demineralized enamel layer. The diffuse-photon density [Fig. 2(a)] decays over the depth of the sample, and the rate of decay increases with increasing value of μ_{a_1}. That is clearly seen from the comparison of the curves in the two enamel layers ($z < 0.8$ mm) and dentin ($z > 0.8$ mm) regions. The assumed absorption coefficient of dentin, $\mu_{a_3} = 400$ m^{-1}, is higher than the absorption coefficients considered for both demineralized and healthy enamel ($\mu_{a_2} = 100$ m^{-1}), so the absorption process is more efficient in the dentin, and the density of available photons decreases here more rapidly as a function of depth. For the very same reason, photon density decreases with increasing value of μ_{a_1} at a fixed depth due to the enhanced de-excitation rate. This difference gradually disappears as photons propagate
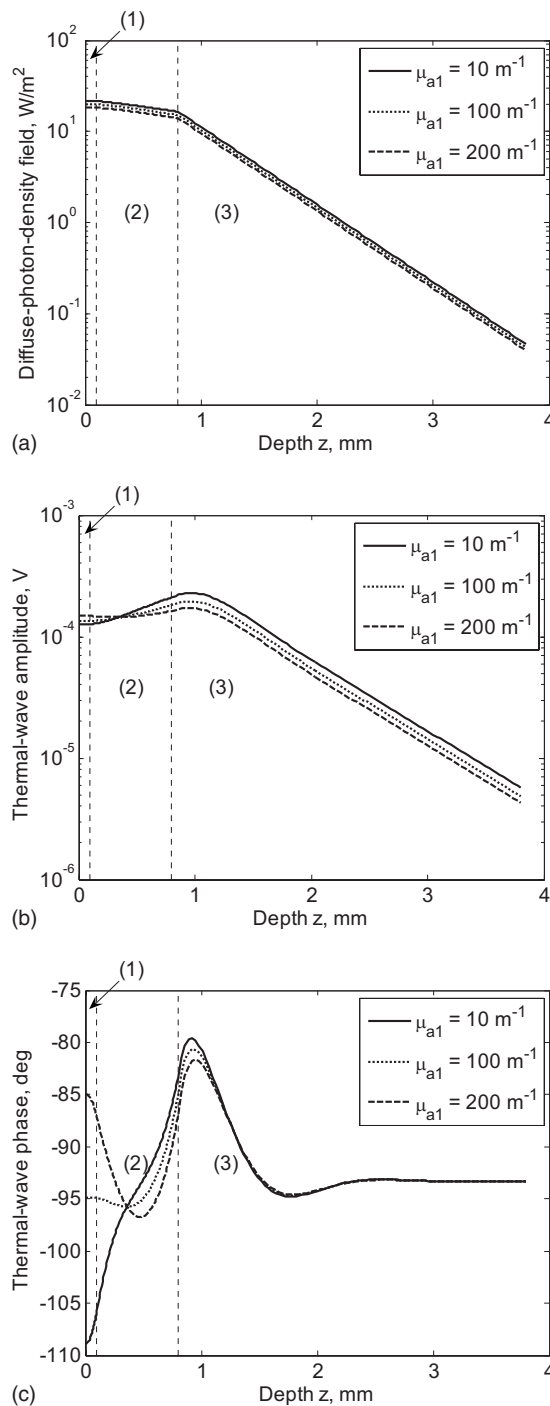

FIG. 2. Photon and thermal-wave field distribution over the distance in an ideally layered tooth: μ_{a_1} variation. The assumed values of other parameters are $\mu_{a_2} = 100$ m^{-1}, $\mu_{a_3} = 400$ m^{-1}, $\mu_{s_1} = 6000$ m^{-1}, $\mu_{s_2} = 6000$ m^{-1}, $\mu_{s_3} = 28\,000$ m^{-1}, $\alpha_1 = 5 \times 10^{-7}$ m^2/s, $\alpha_2 = 5 \times 10^{-7}$ m^2/s, $\alpha_3 = 2 \times 10^{-7}$ m^2/s, $\kappa_1 = 0.9$ W/mK, $\kappa_2 = 0.9$ W/mK, $\kappa_3 = 0.6$ W/mK, $\eta_{NR1} = 0.5$, $\eta_{NR2} = 0.5$, $\eta_{NR3} = 0.5$, $r_{01} = 0.65$, $L_1 = 100$ μm, $L_2 = 700$ μm, $L_3 = 3000$ μm, $R_1 = 0.5$, $R_2 = 0.5$, and $g = 0.96$. Thermal-wave modulation frequency $f = 1$ Hz.

deeper into the enamel, and then are quickly absorbed by the dentin. The corresponding thermal-wave amplitude [Fig. 2(b)] does not decrease monotonically over the sample depth. The amplitude exhibits a local maximum somewhat beyond the enamel-dentin interface, since higher absorption in dentin creates a stronger thermal-wave field. More photons are converted into heat on the other side of the enamel layer and generate an exponentially decreasing thermal-wave

field in region (3) (dentin) as less optical power is transmitted into that medium. At a fixed demineralized enamel (1) depth, the amplitude is higher for higher values of μ_a, since the thermal-wave field source is stronger. At the same time, fewer photons are transmitted farther into the bulk, so the amplitude decreases more rapidly for higher absorption coefficients, which is responsible for the crossover of curves in Fig. 2(a) and appears on a logarithmic scale as a constant offset between the three decreasing curves at deeper regions. The thermal-wave phase [Fig. 2(c)] is more sensitive than the amplitude to the change in absorption coefficient, so the phase lag is smaller for the medium with the higher absorption coefficient, and a crossover behavior, consistent with the changes in the amplitude, is obvious inside the enamel layer. The oscillatory phase shift represents the formation of a standing thermal wave within the enamel layer. An increase in the absorption coefficient of layer (1) confines the subsurface extent of the thermal wave to a narrower region which enhances the interference between forward propagating and interface-interacted thermal waves,[65] resulting in higher peak-to-peak phase interferometric patterns. As expected, for the higher absorption coefficient ($\mu_{a_1}=200$ m^{-1}), the phase lag is smaller, and it increases more steeply from the demineralized region into the healthy enamel than those associated with lower absorption ($\mu_{a_1}=100$ m^{-1} and $\mu_{a_1}=10$ m^{-1}) cases, since photons are absorbed at a higher spatial rate generating a steeper thermal-wave gradient. As photons penetrate the dentin layer, they are efficiently absorbed. The phase oscillations are steadily damped and adjust to local optical properties, becoming independent of μ_{a_1} at depths larger compared to the thermal diffusion length in the dentin.

A more dramatic yet similar behavior is observed for variations in the absorption coefficient of the much thicker healthy enamel layer in region (2), Fig. 3. The assumed thicknesses are $L_1=100$ μm and $L_2=700$ μm, same as in Fig. 2. In this case, the absorption coefficient of the thin demineralized upper layer does not significantly affect the optical field distribution in the healthy region. Thus, with assumed equal values of absorption coefficients of the demineralized layer, the difference between the diffuse-photon-density curves due to the change in values of μ_{a_2} is much more prominent. Fewer photons can penetrate deep into the dentin, and the depth dependence of the diffuse-photon density becomes effectively negligible, although this is not apparent on the logarithmic scale of Fig. 3(a). Similar trends are observed for the thermal-wave curves [Figs. 3(b) and 3(c)]. The influence of absorption on the thermal-wave amplitude in layer (2) is more evident here than in the previous simulation due to the larger differences in optical fluxes in the thick enamel layer. The difference between thermal-wave amplitudes at a given depth within region (2) is further enhanced due to the direct absorption in the more highly absorbing underlying layer [Fig. 3(b)]. The smaller thermal diffusivity of the dentinal layer (3) generates an effective thermal barrier at the dentin-enamel junction (DEJ) resulting in thermal-wave confinement in layer (2) with standing-wave characteristics, as the thickness L_2 (700 μm) is commensurate with the thermal diffusion length l_d (400 μm) in this layer. Phase interference fringes appear which are more pro-
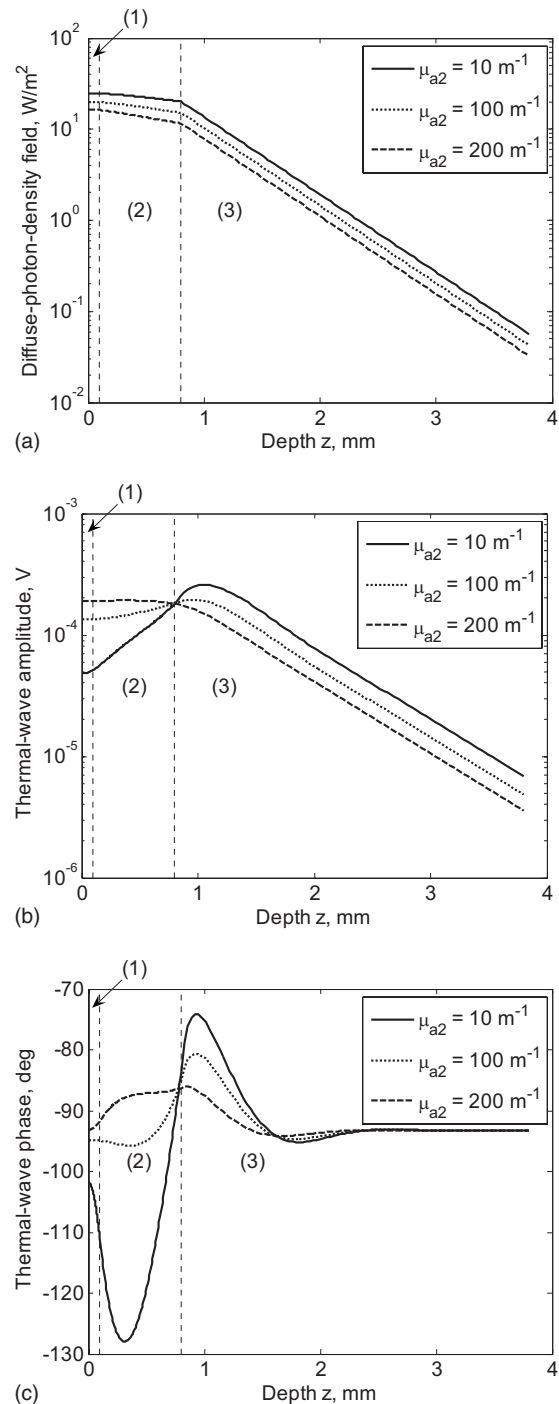

FIG. 3. Photon and thermal-wave field distribution over the distance in an ideally layered tooth: μ_{a_2} variation. The assumed values of other parameters are $\mu_{a_1}=100$ m^{-1}, $\mu_{a_3}=400$ m^{-1}, $\mu_{s_1}=6000$ m^{-1}, $\mu_{s_2}=6000$ m^{-1}, $\mu_{s_3}=28\,000$ m^{-1}, $\alpha_1=5\times10^{-7}$ m^2/s, $\alpha_2=5\times10^{-7}$ m^2/s, $\alpha_3=2\times10^{-7}$ m^2/s, $\kappa_1=0.9$ W/mK, $\kappa_2=0.9$ W/mK, $\kappa_3=0.6$ W/mK, $\eta_{NR1}=0.5$, $\eta_{NR2}=0.5$, $\eta_{NR3}=0.5$, $r_{01}=0.65$, $L_1=100$ μm, $L_2=700$ μm, $L_3=3000$ μm, $R_1=0.5$, $R_2=0.5$, and $g=0.96$. Thermal-wave modulation frequency $f=1$ Hz.

nounced for a more transparent region (2) [Fig. 3(c)], owing to more significant thermal-wave contributions backward from layer (3) into the thermal wave in layer (2). In a more opaque medium in layer (2), the transmitted optical flux is diminished and generates a smaller source in layer (3) and proportionally smaller contribution to the thermal-wave field of layer (2). As expected, the increased absorption coefficient
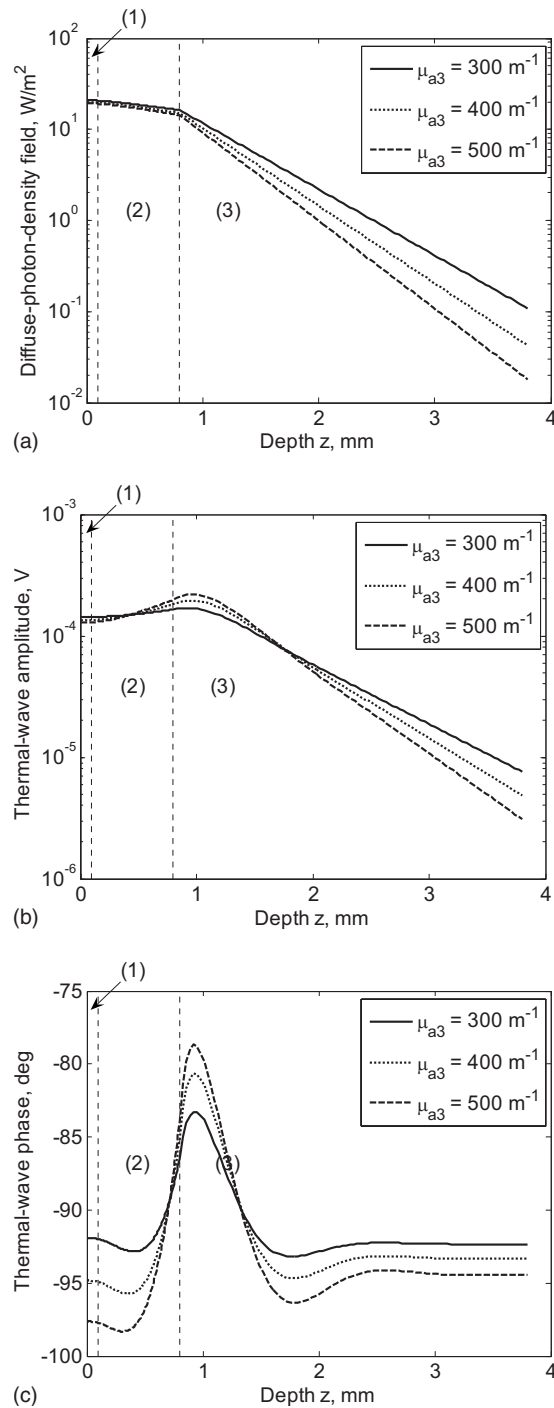
FIG. 4. Photon and thermal-wave field distribution over the distance in an ideally layered tooth: μ_{a_3} variation. The assumed values of other parameters are $\mu_{a_1}=100$ m^{-1}, $\mu_{a_2}=100$ m^{-1}, $\mu_{s_1}=6000$ m^{-1}, $\mu_{s_2}=6000$ m^{-1}, $\mu_{s_3}=28\,000$ m^{-1}, $\alpha_1=5\times10^{-7}$ m^2/s, $\alpha_2=5\times10^{-7}$ m^2/s, $\alpha_3=2\times10^{-7}$ m^2/s, $\kappa_1=0.9$ W/mK, $\kappa_2=0.9$ W/mK, $\kappa_3=0.6$ W/mK, $\eta_{NR1}=0.5$, $\eta_{NR2}=0.5$, $\eta_{NR3}=0.5$, $r_{01}=0.65$, $L_1=100$ μm, $L_2=700$ μm, $L_3=3000$ μm, $R_1=0.5$, $R_2=0.5$, and $g=0.96$. Thermal-wave modulation frequency $f=1$ Hz.

in layer (2) in the latter case results in increased heat conduction to the surface and thermal-wave amplitude enhancement at $z=0$ mm.

Finally, the effects of variations in dentin absorption coefficient on the diffuse-photon and thermal-wave fields are analyzed in Fig. 4. Although the absorption coefficients of both enamel overlayers are the same for all three curves, there is a difference between total diffuse-photon densities in

the enamel region due to the differences in dentinal absorption coefficients [Fig. 4(a)]. A difference in the thermal-wave amplitude behavior in the enamel region [Fig. 4(b)] also exists, although it is not very prominent. Here, increased thermal-wave amplitudes in layer (3) adjacent to the boundary L_2 for increasing μ_{a_3} are expected and observed. At larger depths $z>L_2$, the larger absorption coefficient leads to decreased thermal-wave amplitudes because of decreased penetration and thermal conversion of the optical field. The peak-to-trough shifts of the thermal-wave phases in Fig. 4(c) exhibit stronger interference patterns for the higher dentinal absorption coefficients owing to the better thermal-wave confinement in the overlying enamel region (2). Deep inside the dentin, the phase lag flattens out as thermal-wave interferences due to the presence of the enamel-dentin interface become negligible at depths large compared to the thermal diffusion length. In Fig. 4(c) it is seen that the lower absorption coefficients μ_{a_3} dampen out the thermal-wave field phase oscillation more readily than higher μ_{a_3}; this is due to the fact that the amplitude decay is less damped for higher μ_{a_3} and $z<2$ mm [Fig. 4(b)], thus contributing to the local standing-wave pattern more efficiently. The phases do not converge to the same value, because the different dentinal absorption coefficients result in different positions of the overall thermal-wave centroid at the particular modulation frequency: the highest μ_{a_3} yields the largest phase lag as more contributions to the overall thermal wave originate in the dentinal layer.

B. Depth profile dependence on the optical scattering coefficient

Figure 5 shows the depth profile of the diffuse-photon (a) and the thermal-wave [(b) and (c)] field for various scattering coefficients of the demineralized enamel layer (1) with $R_2=0$ [no back reflectance from the boundary between layers (2) and (3)], which is equivalent to a configuration without internal inter-reflections within the upper layer. The selected μ_s values are typical of the range encountered in hard dental tissues (Table I). The significant changes in scattering properties only slightly affect the diffuse-photon density [Fig. 5(a)]. The corresponding thermal-wave amplitude [Fig. 5(b)] and phase [Fig. 5(c)] are little affected by changes in the demineralized layer scattering coefficient as well. The slight increase in the thermal-wave amplitude and decrease in phase lag with increasing scattering coefficient is due to the enhanced localization of the optical field in the very near-surface region which leads to higher probability for absorption and nonradiative (thermal) energy conversion there. This effect is well known.[49]

The optical and thermal field behaviors change more readily with μ_{s_1} when reflectance at the boundary between the demineralized layer (1) and healthy enamel (2) is taken into account (Fig. 6). Diffuse-photon density increases for smaller scattering coefficients [Fig. 6(a)] since more photons reach the opposite boundary and are reflected, thus increasing the total number of diffuse photons in layer (1). The same reason, upper layer localization, leads to an increase in the thermal-wave amplitude for smaller scattering coeffi-
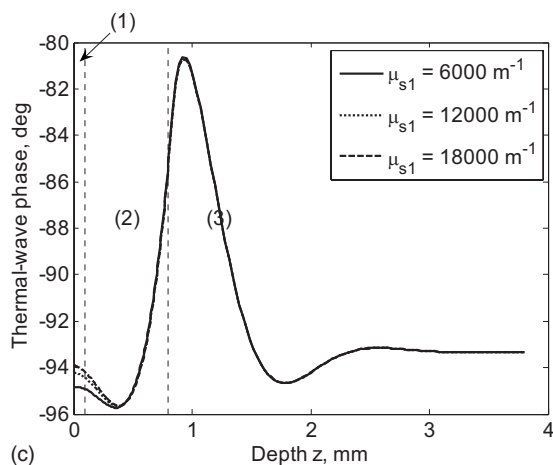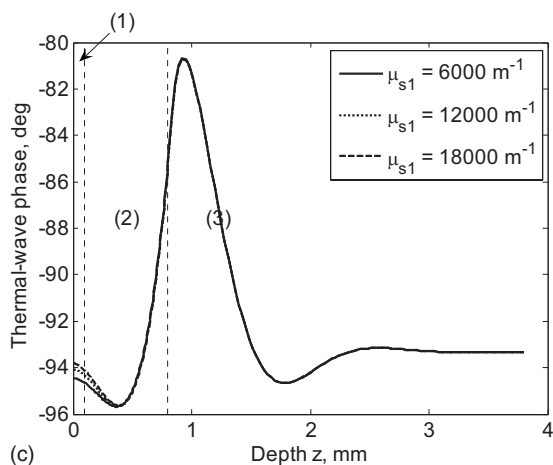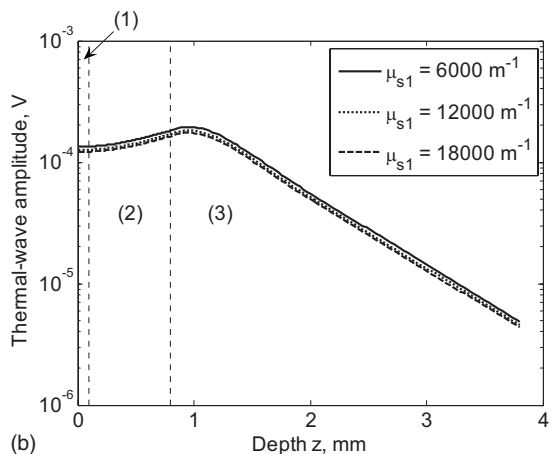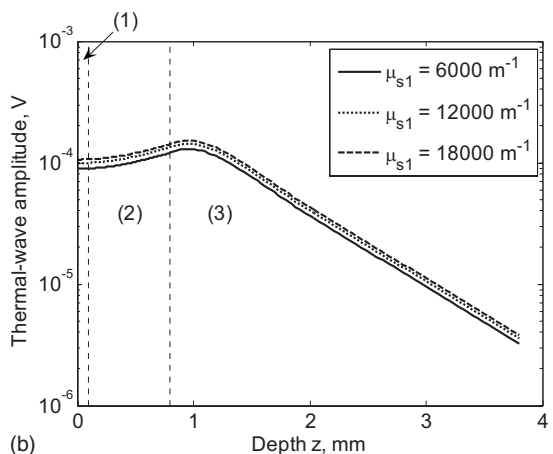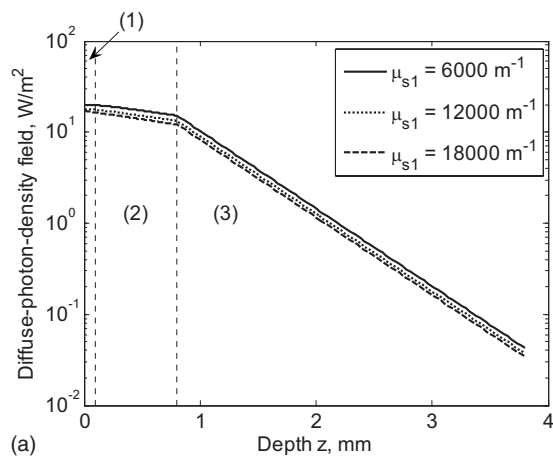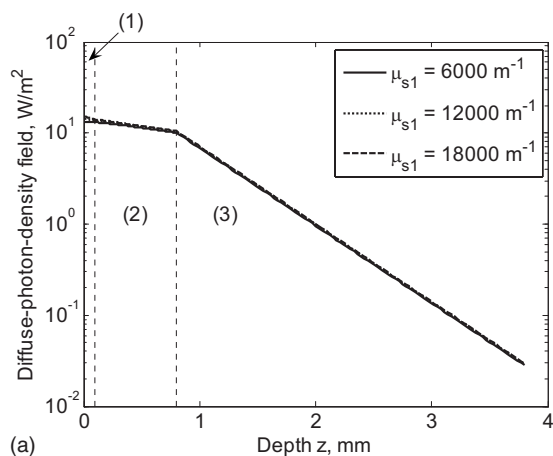
FIG. 5. Photon and thermal-wave field distribution over the distance in an ideally layered tooth: μ_{s_1} variation. The assumed values of other parameters are $\mu_{a_1}=100$ m^{-1}, $\mu_{a_2}=100$ m^{-1}, $\mu_{a_3}=400$ m^{-1}, $\mu_{s_2}=6000$ m^{-1}, $\mu_{s_3}=28\,000$ m^{-1}, $\alpha_1=5\times10^{-7}$ m^2/s, $\alpha_2=5\times10^{-7}$ m^2/s, $\alpha_3=2\times10^{-7}$ m^2/s, $\kappa_1=0.9$ W/mK, $\kappa_2=0.9$ W/mK, $\kappa_3=0.6$ W/mK, $\eta_{NR1}=0.5$, $\eta_{NR2}=0.5$, $\eta_{NR3}=0.5$, $r_{01}=0.65$, $L_1=100$ μm, $L_2=700$ μm, $L_3=3000$ μm, $R_1=0.5$, $R_2=0$, and $g=0.96$. Thermal-wave modulation frequency $f=1$ Hz.

FIG. 6. Photon and thermal-wave field distribution over the distance in an ideally layered tooth: μ_{s_1} variation. The assumed values of other parameters are $\mu_{a_1}=100$ m^{-1}, $\mu_{a_2}=100$ m^{-1}, $\mu_{a_3}=400$ m^{-1}, $\mu_{s_2}=6000$ m^{-1}, $\mu_{s_3}=28\,000$ m^{-1}, $\alpha_1=5\times10^{-7}$ m^2/s, $\alpha_2=5\times10^{-7}$ m^2/s, $\alpha_3=2\times10^{-7}$ m^2/s, $\kappa_1=0.9$ W/mK, $\kappa_2=0.9$ W/mK, $\kappa_3=0.6$ W/mK, $\eta_{NR1}=0.5$, $\eta_{NR2}=0.5$, $\eta_{NR3}=0.5$, $r_{01}=0.65$, $L_1=100$ μm, $L_2=700$ μm, $L_3=3000$ μm, $R_1=0.5$, $R_2=0.5$, and $g=0.96$. Thermal-wave modulation frequency $f=1$ Hz.

cients [Fig. 6(b)]. The phase lag is slightly smaller for larger μ_{s_1} [Fig. 6(c)], as larger μ_{s_1} offers a higher degree of photon localization within layer (1), regardless of the value of R_2, including $R_2=0$ [Fig. 5(c)].

The difference among depth profiles becomes more evident when it comes to changes in the scattering coefficient of the thicker healthy enamel layer (2) (Fig. 7), where the layer

depth is commensurate with the considered optical scattering lengths. The diffuse-photon flux is significantly higher for the higher scattering coefficient, since the enhanced scattering rate localizes the diffuse-photon-density field closer to the surface [Fig. 7(a)]. The photon flux decreases with increasing μ_{s_2}, as expected, in the forward direction from enamel into the dentin layer. In the dentin region, the differ-
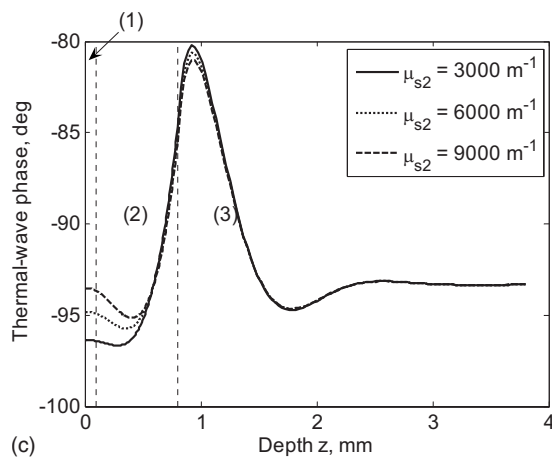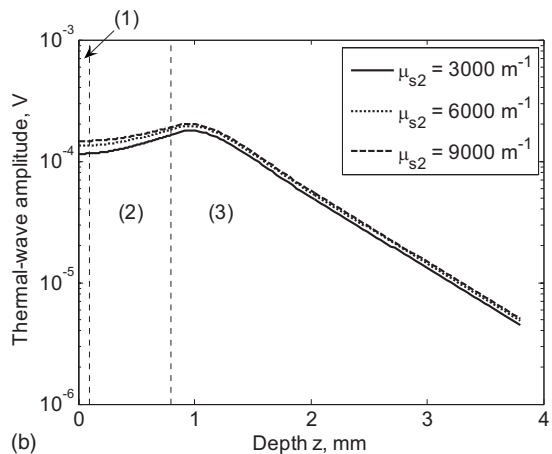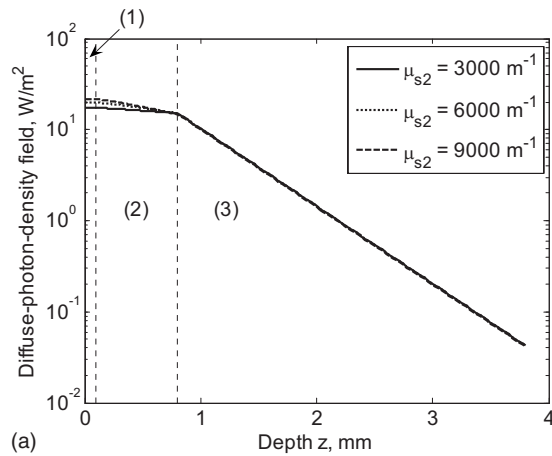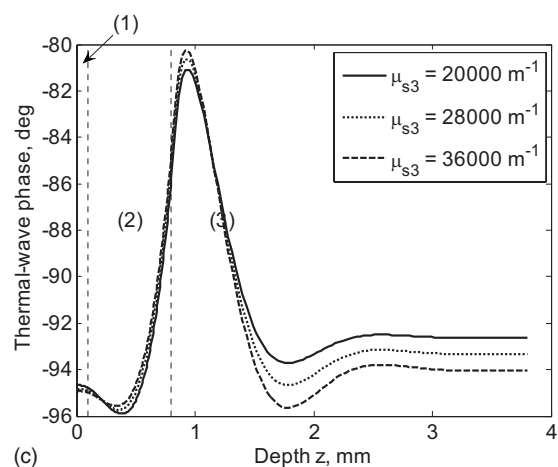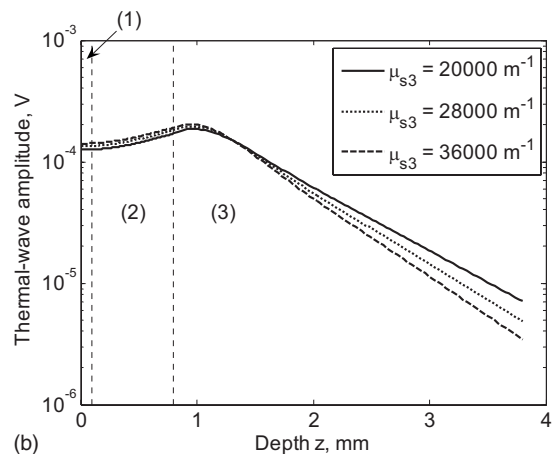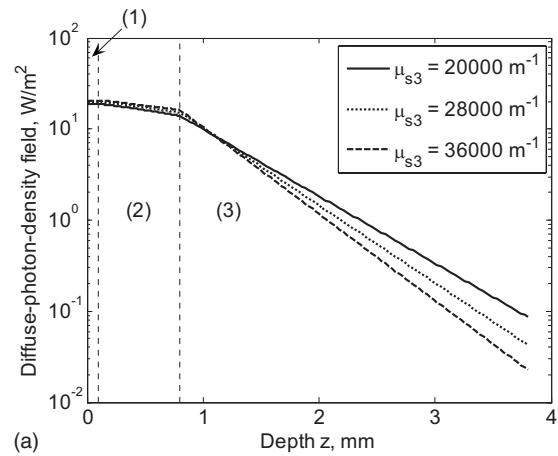
FIG. 7. Photon and thermal-wave field distribution over the distance in an ideally layered tooth: μ_{s_2} variation. The assumed values of other parameters are $\mu_{a_1}=100$ m^{-1}, $\mu_{a_2}=100$ m^{-1}, $\mu_{a_3}=400$ m^{-1}, $\mu_{s_1}=6000$ m^{-1}, $\mu_{s_3}=28\,000$ m^{-1}, $\alpha_1=5\times10^{-7}$ m^2/s, $\alpha_2=5\times10^{-7}$ m^2/s, $\alpha_3=2\times10^{-7}$ m^2/s, $\kappa_1=0.9$ W/mK, $\kappa_2=0.9$ W/mK, $\kappa_3=0.6$ W/mK, $\eta_{NR1}=0.5$, $\eta_{NR2}=0.5$, $\eta_{NR3}=0.5$, $r_{01}=0.65$, $L_1=100$ μm, $L_2=700$ μm, $L_3=3000$ μm, $R_1=0.5$, $R_2=0.5$, and $g=0.96$. Thermal-wave modulation frequency $f=1$ Hz.

FIG. 8. Photon and thermal-wave field distribution over the distance in an ideally layered tooth: μ_{s_3} variation. The assumed values of other parameters are $\mu_{a_1}=100$ m^{-1}, $\mu_{a_2}=100$ m^{-1}, $\mu_{a_3}=400$ m^{-1}, $\mu_{s_1}=6000$ m^{-1}, $\mu_{s_2}=6000$ m^{-1}, $\alpha_1=5\times10^{-7}$ m^2/s, $\alpha_2=5\times10^{-7}$ m^2/s, $\alpha_3=2\times10^{-7}$ m^2/s, $\kappa_1=0.9$ W/mK, $\kappa_2=0.9$ W/mK, $\kappa_3=0.6$ W/mK, $\eta_{NR1}=0.5$, $\eta_{NR2}=0.5$, $\eta_{NR3}=0.5$, $r_{01}=0.65$, $L_1=100$ μm, $L_2=700$ μm, $L_3=3000$ μm, $R_1=0.5$, $R_2=0.5$, and $g=0.96$. Thermal-wave modulation frequency $f=1$ Hz.

ences caused by the change in the enamel scattering properties are not apparent, since the scattering coefficient of dentin, μ_{s_3}, is 28 000 m^{-1}, much larger than the change in enamel scattering coefficient. In this case, photons entering the dentinal region are much more intensely scattered, thus quickly losing memory of any initial field differences at the enamel-air boundary. The increase in the enamel scattering coefficient slightly increases the thermal-wave amplitude

[Fig. 7(b)] due to enhanced localization and probability for absorption closer to the surface. The same reason accounts for the smallest phase lag at the surface for the largest μ_{s_2} [Fig. 7(c)]. The peak-to-trough oscillation of the thermal-wave phase interference pattern within the dentin layer slightly decreases with increasing μ_{s_2}, as less optical flux reaches layer (3) to generate a weaker thermal-wave source
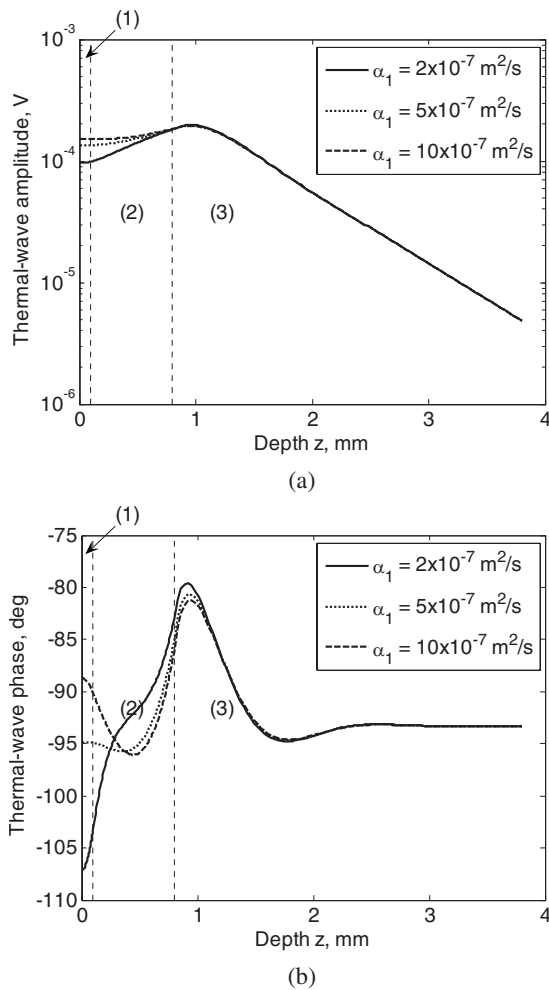
(a)

(b)

FIG. 9. Thermal-wave field distribution over the distance in an ideally layered tooth: α_1 variation. The assumed values of other parameters are μ_{a_1} =100 m^{-1}, μ_{a_2}=100 m^{-1}, μ_{a_3}=400 m^{-1}, μ_{s_1}=6000 m^{-1}, μ_{s_2}=6000 m^{-1}, μ_{s_3}=28 000 m^{-1}, α_2=5$\times$10^{-7} m^2/s, α_3=2$\times$10^{-7} m^2/s, κ_1=0.9 W/mK, κ_2=0.9 W/mK, κ_3=0.6 W/mK, η_{NR1}=0.5, η_{NR2}=0.5, η_{NR3}=0.5, r_{01} =0.65, L_1=100 μm, L_2=700 μm, L_3=3000 μm, R_1=0.5, R_2=0.5, and g =0.96. Thermal-wave modulation frequency f=1 Hz.
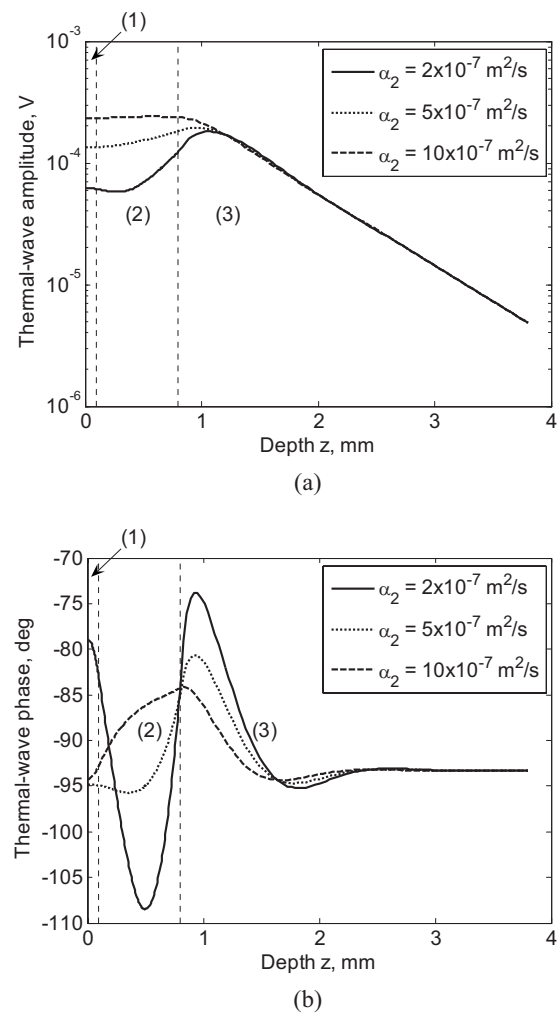

(a)

(b)

FIG. 10. Thermal-wave field distribution over the distance in an ideally layered tooth: α_2 variation. The assumed values of other parameters are μ_{a_1}=100 m^{-1}, μ_{a_2}=100 m^{-1}, μ_{a_3}=400 m^{-1}, μ_{s_1}=6000 m^{-1}, μ_{s_2} =6000 m^{-1}, μ_{s_3}=28 000 m^{-1}, α_1=5$\times$10^{-7} m^2/s, α_3=2$\times$10^{-7} m^2/s, κ_1 =0.9 W/mK, κ_2=0.9 W/mK, κ_3=0.6 W/mK, η_{NR1}=0.5, η_{NR2}=0.5, η_{NR3}=0.5, r_{01}=0.65, L_1=100 μm, L_2=700 μm, L_3=3000 μm, R_1=0.5, R_2=0.5, and g=0.96. Thermal-wave modulation frequency f=1 Hz.

upon absorption, which subsequently diffuses across the boundary L_2 and interferes with the forward diffusing thermal wave generated in layer (2). Increased μ_{s_2} ultimately leads to a thermal-wave centroid located closer to the surface of the layered structure and a smaller phase lag which can be used as a simple diagnostic of increased scattering in the near-surface region of human teeth (e.g., due to hypermineralization lesions).

Variations in dentin scattering coefficient lead to more pronounced changes in both diffuse-photon-density flux and thermal-wave field (Fig. 8). Although the scattering coefficient of enamel is not varied, the diffuse-photon density of enamel increases when the scattering coefficient of dentin increases, owing to enhanced back-scattered photon flux from the dentin back into the enamel. This trend is similar to dentin absorption depth profiles shown in Fig. 4(a) and has a similar explanation in the form of overall optical flux increased attenuation with increased μ_{s_3}. As a result, the thermal-wave amplitude decrease in layer (3) [Fig. 8(b)] is steeper for higher μ_{s_3}, as expected from the decreased optical

source in dentin [Fig. 8(a)]. The back-scattered photons, which produce a higher photon density within layers (1) and (2) with increased μ_{s_3}, also result in a higher thermal-wave amplitude in those regions [Fig. 8(b)]. The thermal-wave phase [Fig. 8(c)] also exhibits significant differences in the dentinal area with scattering coefficient, μ_{s_3}, variation. In a manner similar to the overall photothermal behavior of the three-layer structure under variations in μ_{a_3} (Fig. 4), an increase in scattering coefficient μ_{s_3} localizes the thermal-wave centroid closer to the L_2 interface, thus contributing more efficiently to the local standing thermal-wave pattern and increasing the peak-to-trough oscillation of the phase lag within the dentin, as shown in Fig. 8(c). This is the result of the increased optical (and thermal) gradient between the DEJ and the dentinal bulk [Figs. 8(a) and 8(b)], thus contributing to an enhanced phase interference fringe.

In summary, the overall analysis of the foregoing simulations shows that the influence of the absorption coefficient on the thermal-wave profiles is more pronounced than the influence of the scattering coefficient of the layers. This de-
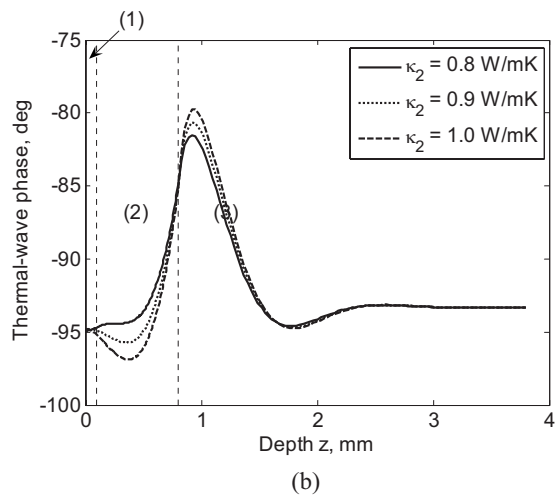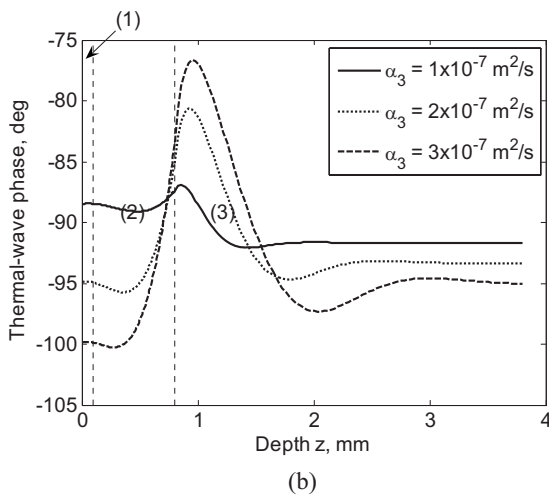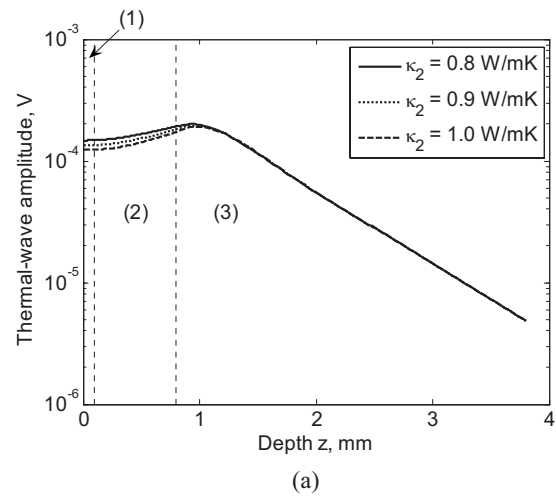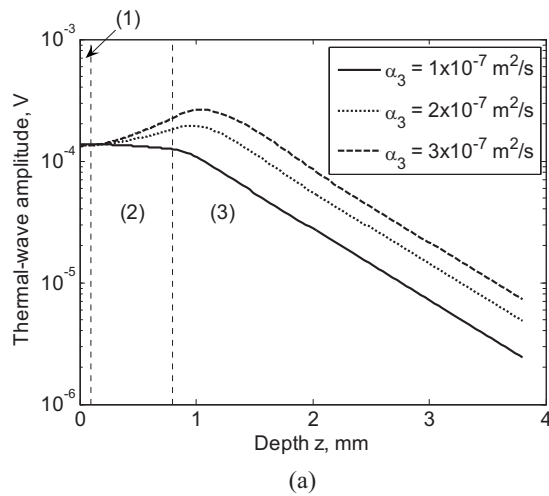
FIG. 11. Thermal-wave field distribution over the distance in an ideally layered tooth: α_3 variation. The assumed values of other parameters are $\mu_{a_1}=100$ m^{-1}, $\mu_{a_2}=100$ m^{-1}, $\mu_{a_3}=400$ m^{-1}, $\mu_{s_1}=6000$ m^{-1}, $\mu_{s_2}=6000$ m^{-1}, $\mu_{s_3}=28\,000$ m^{-1}, $\alpha_1=5\times10^{-7}$ m^2/s, $\alpha_2=5\times10^{-7}$ m^2/s, $\kappa_1=0.9$ W/mK, $\kappa_2=0.9$ W/mK, $\kappa_3=0.6$ W/mK, $\eta_{NR1}=0.5$, $\eta_{NR2}=0.5$, $\eta_{NR3}=0.5$, $r_{01}=0.65$, $L_1=100$ μm, $L_2=700$ μm, $L_3=3000$ μm, $R_1=0.5$, $R_2=0.5$, and $g=0.96$. Thermal-wave modulation frequency $f=1$ Hz.

FIG. 12. Thermal-wave field distribution over the distance in an ideally layered tooth: κ_2 variation. The assumed values of other parameters are $\mu_{a_1}=100$ m^{-1}, $\mu_{a_2}=100$ m^{-1}, $\mu_{a_3}=400$ m^{-1}, $\mu_{s_1}=6000$ m^{-1}, $\mu_{s_2}=6000$ m^{-1}, $\mu_{s_3}=28\,000$ m^{-1}, $\alpha_1=5\times10^{-7}$ m^2/s, $\alpha_2=5\times10^{-7}$ m^2/s, $\alpha_3=2\times10^{-7}$ m^2/s, $\kappa_1=0.9$ W/mK, $\kappa_3=0.6$ W/mK, $\eta_{NR1}=0.5$, $\eta_{NR2}=0.5$, $\eta_{NR3}=0.5$, $r_{01}=0.65$, $L_1=100$ μm, $L_2=700$ μm, $L_3=3000$ μm, $R_1=0.5$, $R_2=0.5$, and $g=0.96$. Thermal-wave modulation frequency $f=1$ Hz.

pendence is also sensitive to the thickness of the layers, since photon diffusion and conversion phenomena have strongly depth-dependent nature. However, the scattering coefficient can still be an important parameter in the analysis of the thin demineralized layers. In this case the optical penetration depth can become comparable to the thickness of the layer and lead to inter-reflections within the layer.

C. Depth profile dependence on thermal diffusivities and thermal conductivities

Another important aspect of the thermal-wave field propagation in dental structures is the influence of the thermophysical parameters. Unlike in homogeneous opaque solids, the depth profile of the thermal-wave amplitude exhibits an increase with increasing thermal diffusivity of the demineralized enamel, layer (1) [Fig. 9(a)]. This increase is caused by the fact that the subsurface thermal-wave sources in layers (2) and (3), upon direct optical absorption and nonradiative conversion in the bulk, can contribute more effi-

ciently to heat diffusion from bulk to surface and raise the thermal-wave amplitude with increased α_1. The thermal-wave phase lag for larger diffusivity [Fig. 9(b)] is smaller at $z=0$ and nearby depths, due to the enhanced back-propagated thermal-wave diffusion from subsurface absorptions, so that the thermal-wave centroid shifts closer to the surface.

The same change in the thermal diffusivity of the relatively thick enamel layer [Fig. 10] leads to much more significant changes in the enamel thermal-wave depth profile. The smaller α_2 impedes back-diffused dentinal thermal-wave contributions (where optical absorption is stronger, $\mu_{a_3}>\mu_{a_2}$, and thermal diffusivity is lower, $\alpha_2>\alpha_3$) from reaching the surface, thus localizing the back-propagated thermal-wave field in layer (2). Figure 10(b) shows the enhanced standing thermal-wave phase pattern for the lowest α_2 and the weakened interference as α_2 increases.

When the dentin thermal diffusivity varies [Fig. 11], the same trends appear: thermal-wave amplitude increases with increasing α_3 and so do the forward- and back-diffused fluxes into layers (3) and (2), respectively [Fig. 11(a)]. The
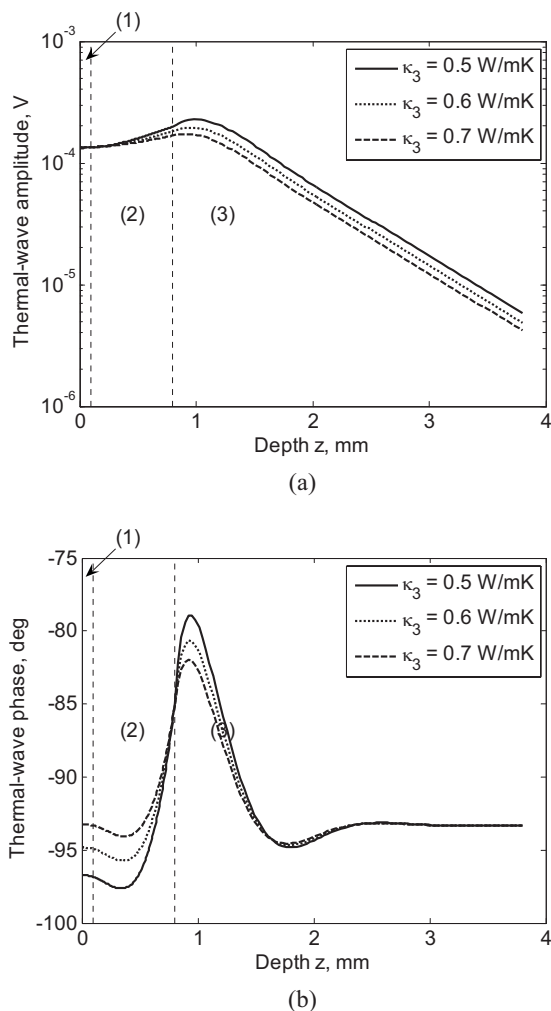
FIG. 13. Thermal-wave field distribution over the distance in an ideally layered tooth: κ_3 variation. The assumed values of other parameters are $\mu_{a_1}=100$ m^{-1}, $\mu_{a_2}=100$ m^{-1}, $\mu_{a_3}=400$ m^{-1}, $\mu_{s_1}=6000$ m^{-1}, $\mu_{s_2}=6000$ m^{-1}, $\mu_{s_3}=28\,000$ m^{-1}, $\alpha_1=5\times10^{-7}$ m^2/s, $\alpha_2=5\times10^{-7}$ m^2/s, $\alpha_3=2\times10^{-7}$ m^2/s, $\kappa_1=0.9$ W/mK, $\kappa_2=0.9$ W/mK, $\eta_{NR1}=0.5$, $\eta_{NR2}=0.5$, $\eta_{NR3}=0.5$, $r_{01}=0.65$, $L_1=100$ μm, $L_2=700$ μm, $L_3=3000$ μm, $R_1=0.5$, $R_2=0.5$, and $g=0.96$. Thermal-wave modulation frequency $f=1$ Hz.

phase behavior is also consistent with the dependence on thermal diffusivity. More coherent thermal-wave flux enters the more thermally conducting enamel region from the highly absorbing dentin to form stronger interference patterns for larger α_3, as the dentin barrier acts as a more highly conducting thermal-wave source. The fact that increased thermal flux arrives at the surface from deeper regions within layer (3) with increasing α_3 shifts the overall thermal-wave centroid away from the surface and increases the phase lag at $z=0$ [Fig. 11(b)].

The change in thermal conductivity of the demineralized layer does not measurably affect the thermal-wave field. That is expected due to its small thickness. However, with the conductivity variation in the thicker healthy enamel, depth profile changes are more prominent (Fig. 12). For lower thermal conductivity, less thermal-wave power is transported forward into the layered structure under the optically imposed thermal-wave gradient, so the thermal-wave amplitude is somewhat larger [Fig. 12(a)]. The increase in thermal conductivity facilitates thermal energy propagation and interfer-

ence between forward and L_2 interface-interacted (back-propagating) thermal waves. Therefore, the strength of the thermal-wave phase standing wave increases somewhat [Fig. 12(b)].

The thermal-wave amplitude decreases in the dentin [Fig. 13(a)] with increased thermal conductivity, as expected. This effect is opposite to that of thermal diffusivity variations, because increased conductivity spreads the available thermal-wave flux across a larger volume. As a result, the thermal-wave phase [Fig. 13(b)] exhibits weaker standing-wave interference patterns with increasing κ_3, which is also opposite from the effect of increasing α_3 [Fig. 11(b)].

The foregoing thermophysical simulations demonstrated the very significant influence of changes in the thermal diffusivity of the layers, while thermal conductivity affected the depth profiles more moderately. This phenomenon can be explained by the exponential dependence of the thermal-wave profiles on the thermal diffusivity, which makes this parameter very important in controlling the behavior of the thermal-wave field.

IV. CONCLUSIONS

In conclusion, the presented theoretical model describes the physics of optical and thermal-wave depth profile behavior in multilayer dental structures, and quantifies the influence of optical parameters, thermal parameters, and interplay between the layers on the depth profiles.

ACKNOWLEDGMENTS

[1] A. Ishimaru, Appl. Opt. **28**, 2210 (1989).
[2] A. Ishimaru, Y. Kuga, R. L. T. Cheung, and K. Shimizu, J. Opt. Soc. Am. **73**, 131 (1983).
[3] P. Kubelka, J. Opt. Soc. Am. **38**, 448 (1948).
[4] R. R. Anderson and J. A. Parrish, J. Invest. Dermatol. **77**, 13 (1981).
[5] S. A. Prahl, M. J. C. van Gemert, and A. J. Welsh, Appl. Opt. **32**, 559 (1993).
[6] J. F. Beek, P. Blokland, P. Posthumus, M. Aalders, J. W. Pickering, H. J. Sterenborg, and M. J. van Gemert, Phys. Med. Biol. **42**, 2255 (1997).
[7] T. L. Troy and S. N. Thennadil, J. Biomed. Opt. **6**, 167 (2001).
[8] A. N. Bashkatov, E. A. Genina, V. I. Kochubey, and V. V. Tuchin, J. Phys. D **38**, 2543 (2005).
[9] S. C. Gebhart, W. C. Lin, and A. Mahadevan-Jansen, Phys. Med. Biol. **51**, 2011 (2006).
[10] E. D. Cashwell and C. J. Everett, *Monte Carlo Method for Random Walk Problems* (Pergamon, London, 1959).
[11] B. C. Wilson and G. Adam, Med. Phys. **10**, 824 (1983).
[12] P. Marquet, F. Bevilacqua, C. Depeursinge, and E. B. de Haller, Opt. Eng. (Bellingham) **34**, 2055 (1995).
[13] A. N. Yaroslavsky, P. C. Schulze, I. V. Yaroslavsky, R. Schober, F. Ulrich, and H. J. Schwartzmaier, Phys. Med. Biol. **47**, 2059 (2002).
[14] R. F. Bonner, R. Nossal, S. Halvin, and G. H. Weiss, J. Opt. Soc. Am. A **4**, 423 (1987).
[15] J. A. Kang, *Electromagnetic Wave Theory* (Wiley, New York, 1986).
[16] P. R. Bargo, S. A. Prahl, T. T. Goodell, R. A. Sleven, G. Koval, G. Blair, and S. L. Jaques, J. Biomed. Opt. **10**, 034018 (2005).
[17] L. Cummins and M. Nauenberg, Biophys. J. **42**, 99 (1983).
[18] G. Yoon, A. J. Welch, M. Motamedi, and M. C. J. van Gemert, IEEE J. Quantum Electron. **QE-23**, 1721 (1987).

[19]R. A. J. Groenhuis, H. A. Ferwerda, and J. J. Ten Bosch, Appl. Opt. **22**, 2456 (1983).

[20]T. J. Farrell, M. S. Patterson, and B. Wilson, Med. Phys. **19**, 879 (1992).

[21]R. Graaff, A. C. M. Dassel, M. H. Koelink, F. F. M. de Mul, J. G. Aarnoudse, and W. G. Zijlstra, Appl. Opt. **32**, 435 (1993).

[22]K. M. Yoo, F. Liu, and R. R. Alfano, J. Opt. Soc. Am. B **7**, 1685 (1990).

[23]M. S. Patterson, J. D. Moulton, B. C. Wilson, K. W. Berndt, and J. R. Lakowicz, Appl. Opt. **30**, 4474 (1991).

[24]C. E. W. Gributs and D. H. Burns, Can. J. Anal. Sci. Spectrosc. **49**, 193 (2004).

[25]M. S. Patterson, B. Chance, and B. C. Wilson, Appl. Opt. **28**, 2331 (1989).

[26]A. A. Oraevsky, S. L. Jaques, and F. K. Tittel, Appl. Opt. **36**, 402 (1997).

[27]P. S. Grashin, A. A. Karabutov, A. A. Oraevsky, I. M. Pelivanov, N. V. Podymova, E. V. Savateeva, and V. S. Solomatin, IEEE J. Quantum Electron. **32**, 868 (2002).

[28]R. R. Anderson, H. Beck, U. Bruggemann, W. Farinelli, S. L. Jaques, and J. A. Parrish, Appl. Opt. **28**, 2256 (1989).

[29]S. A. Prahl, I. A. Vitkin, U. Bruggemann, B. C. Wilson, and R. R. Anderson, Phys. Med. Biol. **37**, 1203 (1992).

[30]S. L. Jaques, J. S. Nelson, W. H. Wright, and T. E. Milner, Appl. Opt. **32**, 2439 (1993).

[31]L. O. Svaasand, B. J. Tromberg, R. C. Haskell, T. T. Tsay, and M. W. Berns, Opt. Eng. **32**, 258 (1993).

[32]L. Nicolaides, A. Mandelis, and S. H. Abrams, J. Biomed. Opt. **5**, 31 (2000).

[33]L. Nicolaides, C. Feng, A. Mandelis, and S. H. Abrams, Appl. Opt. **41**, 768 (2002).

[34]D. Fried, W. Seka, R. E. Glena, and J. D. B. Featherstone, Opt. Eng. (Bellingham) **35**, 1976 (1996).

[35]M. J. Zuerlein, D. Fried, J. D. B. Featherstone, and W. Seka, IEEE J. Quantum Electron. **5**, 1083 (1999).

[36]A. Mandelis, Phys. Today **53**, 29 (2000).

[37]A. Yodh and B. Chance, Phys. Today **48**, 34 (1995).

[38]A. Mandelis, *Diffusion Wave Fields: Mathematical Methods and Green Functions* (Springer, New York, 2001).

[39]M. A. O'Leary, D. A. Boas, B. Chance, and A. G. Yodh, Phys. Rev. Lett. **69**, 2658 (1992).

[40]D. A. Boas, M. A. O'Leary, B. Chance, and A. G. Yodh, Appl. Opt. **36**, 75 (1997).

[41]B. J. Tromberg, L. O. Svaasand, T. Tsay, and R. C. Haskell, Appl. Opt. **32**, 607 (1993).

[42]J. B. Fishkin and E. Gratton, J. Opt. Soc. Am. A **10**, 127 (1993).

[43]J. M. Schmitt, A. Knuttel, and R. J. Knutson, J. Opt. Soc. Am. A **9**, 1832 (1992).

[44]L. Nicolaides, Y. Chan, A. Mandelis, and I. A. Vitkin, J. Opt. Soc. Am. A Opt. Image Sci. Vis. **18**, 2548 (2001).

[45]D. Fried, R. E. Glena, J. D. B. Featherstone, and W. Seka, Appl. Opt. **34**, 1278 (1995).

[46]C. L. Darling, G. D. Huynh, and D. Fried, J. Biomed. Opt. **11**, 034023 (2006).

[47]S. A. Telenkov, J. I. Youn, D. M. Goodman, A. J. Welch, and T. E. Milner, Phys. Med. Biol. **46**, 551 (2001).

[48]G. T. Anderson, J. W. Valvano, and R. R. Santos, IEEE Trans. Biomed. Eng. **39**, 877 (1992).

[49]A. Mandelis and C. Feng, Phys. Rev. E **65**, 021909 (2002).

[50]J. M. Schmitt, G. X. Zhou, E. C. Walker, and R. T. Wall, J. Opt. Soc. Am. A **7**, 2141 (1990).

[51]L. O. Svaasand, T. Spott, J. B. Fishkin, T. Pham, B. J. Tromberg, and M. W. Berns, Phys. Med. Biol. **44**, 801 (1999).

[52]A. Kienle, M. S. Patterson, N. Dognitz, R. Bays, G. Wagnieres, and H. van den Bergh, Appl. Opt. **37**, 779 (1998).

[53]A. D. Kim and M. Moscoso, J. Biomed. Opt. **10**, 034015 (2005).

[54]H. Taitelbaum, S. Havlin, and G. H. Weiss, Appl. Opt. **28**, 2245 (1989).

[55]X. Deulin and J. P. L'Huillier, Eur. Phys. J.: Appl. Phys. **33**, 133 (2006).

[56]T. J. Farrell, M. S. Patterson, and M. Essenpreis, Appl. Opt. **37**, 1958 (1998).

[57]G. Alexandrakis, T. J. Farrell, and M. S. Patterson, Appl. Opt. **37**, 7401 (1998).

[58]X. Wang, Y. Gong, D. C. Song, and Z. Wu, Int. J. Infrared Millim. Waves **25**, 1545 (2004).

[59]A. Kienle, T. Glanzmann, G. Wagnieres, and H. van den Bergh, Appl. Opt. **37**, 6852 (1998).

[60]T. M. Smith, A. J. Olejniczak, D. J. Reid, R. J. Ferrell, and J. J. Hublin, Arch. Oral Biol. **51**, 974 (2006).

[61]J. L. Stroud, P. H. Buschang, and P. W. Goaz, Dentomaxillofac Radiol. **23**, 169 (1994).

[62]R. J. Jeon, A. Matvienko, A. Mandelis, S. H. Abrams, B. T. Amaechi, and G. Kulkarni, J. Biomed. Opt. **12**, 034028 (2007).

[63]W. S. Brown, W. A. Dewey, and H. R. Jacobs, J. Dent. Res. **49**, 752 (1970).

[64]M. Braden, Arch. Oral Biol. **9**, 479 (1964).

[65]A. Mandelis, L. Nicolaides, and Y. Chen, Phys. Rev. Lett. **87**, 020801 (2001).